SUPPORTING INFORMATION: INFLUENCE OF COMPENSATING DEFECT FORMATION ON THE DOPING EFFICIENCY AND THERMOELECTRIC PROPERTIES OF $Cu_{2-y}Se_{1-x}Br_x$

X-ray diffraction data modeling. Powder diffraction patterns were modeled using a small, anorthic unit cell derived from a LP search (TOPAS Academic V4.1). Figure S1 shows the x-ray powder diffraction data of the synthesized $Cu_{2-\delta}Se$ with the corresponding Pawley fit. A triclinic unit cell with a = 7.082(8) Å, b = 4.121(3) Å, c = 7.121(3) Å, α = 106.1(0), β = 99.1(0)° and γ = 90.1(4)° has been utilized for the fits in order to determine lattice parameters for each composition.

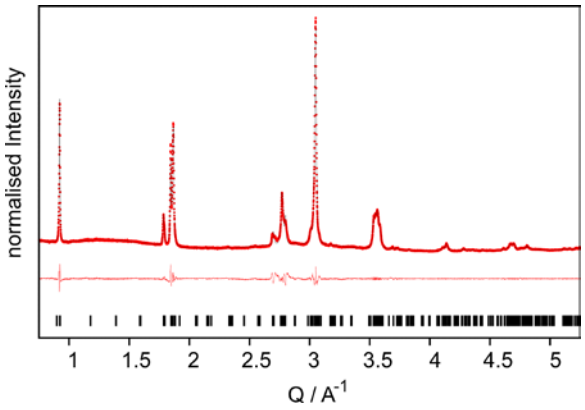

Figure S1. Exemplary x-ray powder diffraction data for $Cu_{2-\delta}Se$ (red dots), including profile fit (black solid line) and profile difference (red solid line) from the corresponding Pawley Fit. Reflections could be indexed to a triclinic unit cell with phase with a = 7.082(8) Å, b = 4.121(3) Å, c = 7.121(3) Å, α = 106.1(0), β = 99.1(0)° and γ = 90.1(4)°, R_{wp}=5.9 % and GoF=2.1.

X-ray diffraction data of $Cu_{2-y}Se_{1-x}Br_x$ with x > 0.05. Besides $Cu_{2-y}Se_{1-x}Br_x$ samples with a substitution grade of selenium versus bromine up to 5 % additional samples have been prepared with a substitution grades of 6 to 10 %. X-ray powder diffraction data of these samples is shown in Figure S2.

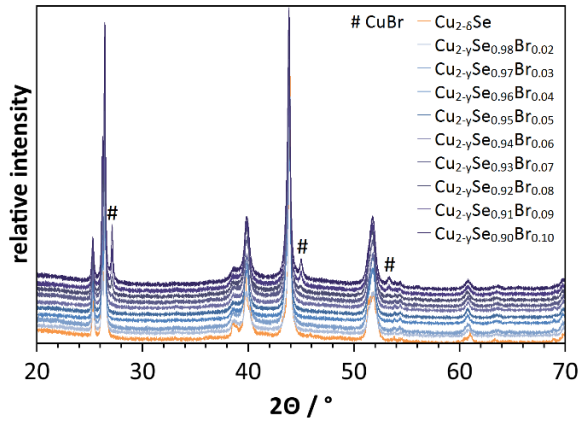

Figure S2. Room temperature X-ray powder diffraction data of the synthesized $Cu_{2-y}Se_{1-x}Br_x$ with the formal composition $Cu_{2-y}Se_{1-x}Br_x$ (x = 0.00, 0.02, 0.03, 0.04, 0.05, 0.06, 0.07, 0.08, 0.09, 0.10). Samples with a substitution grade from 7 to 10 % show additional reflections (#), which can be attributed to a CuBr impurity phase (#).

Unfortunately these samples are not single phase as data from the samples with a substitution grade from 7 to 10 % show reflections of CuBr. In order to rule out phase segregation influences on the transport properties the samples from 6 to 10 % have not been further investigated with respect to thermoelectric properties.

Experimental-XPS. The powdered samples were pressed into pellets and the surface was sputtered by 3 keV electron gun for 120 seconds in order to remove the native oxides before measuring. The oxygen 1s peaks of both the samples were completely removed after sputtering.

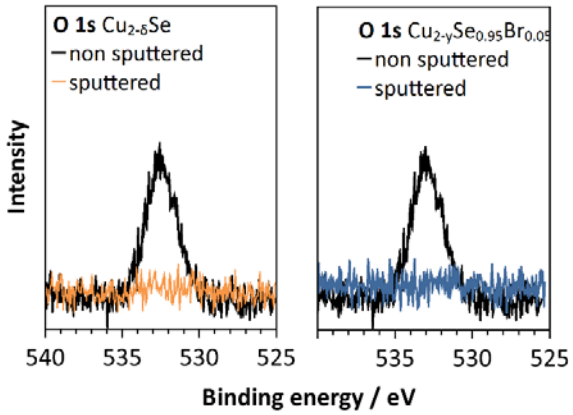

Figure S3a. Oxygen 1s peak in the XPS spectra for $Cu_{2-\delta}Se$ (left) and $Cu_{2-y}Se_{0.95}Br_{0.05}$ (right) before and after sputtering for 120 seconds in order to remove native oxides.

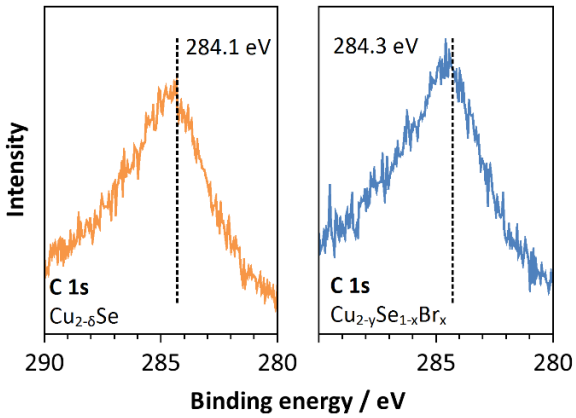

Figure S3b. Carbon 1s peak in the XPS spectra (binding energy 284.5 eV) for $Cu_{2-\delta}Se$ (left) and $Cu_{2-y}Se_{0.95}Br_{0.05}$ (right), which was used as a reference to calibrate the binding energies of the other core level spectra.

XRF. X-ray fluorescence (XRF) analysis was used to obtain a precise atomic percent ratio of bromine to selenium in each synthesized $Cu_{2-y}Se_{1-x}Br_x$ sample. These ratios were determined by using: 1) the measured Se Kα (11.2 keV) and Br Kα (11.9 keV) net photon counts from the solid-state detector XRF spectra (Figure S4), 2) the cross-sections for these XRF emission lines at the incident energy of 17.4 keV,[I] 3) the calculated transmissions for the incident and emitted X-rays in the sample, 4) the transmissions for the emitted X-rays through the air path between the sample and the detector, and 5) the detector efficiency.

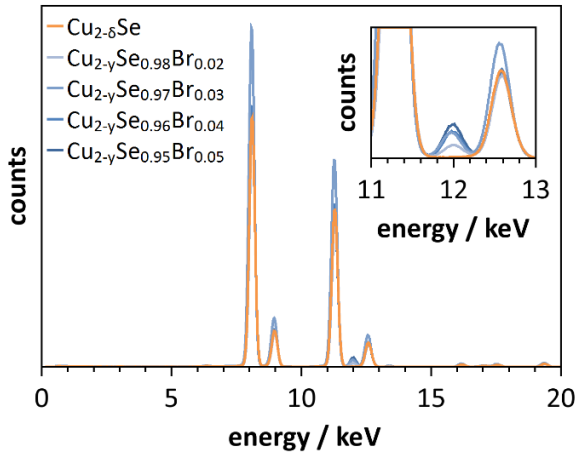

Figure S4. XRF spectra for the investigated copper selenide samples.

ICP-MS. The variation of the Cu/Se ratio was determined with ICP-MS. Data were obtained by dissolving 50 mg of the powdered samples in conc. HNO_3 (Merck, Suprapure). The obtained solutions were diluted to the required concentration of 10-100 ppb Cu and Se. As internal standard 5ppb Rh were added. The measured isotopes were Cu(63), Cu(65), Se(77), Br(79) and Rh(103). Table S1 lists the operating parameters for the ICP mass spectrometer. Typical signal intensities were 1.6-2.7 × 10^7 with 1.0-2.1 × 10^5 blind count rates for Cu(65), 3.0-6.0 × 10^5 with 4.7-5.4 × 10^3 blind count rates for Se(77) and 8.2-4.3 × 10^6 for Rh(103).

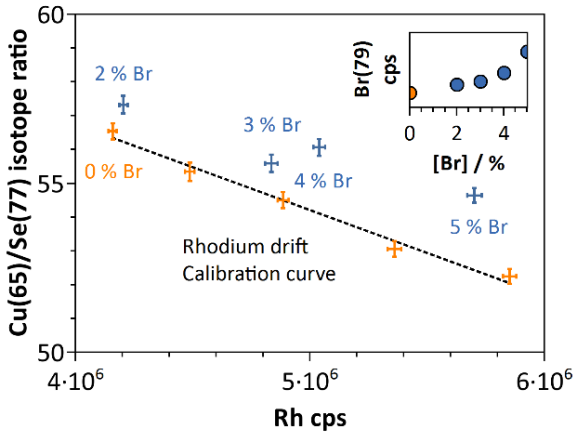

Figure S5. Linear calibration curve of the Cu(65)/Se(77) ratio versus the absolute Rh(103) count rate for the $Cu_{2-\delta}Se$ sample (black dotted line). Orange dots represent measurements of the undoped $Cu_{2-\delta}Se$ sample which were used to obtain the calibration curve, blue dots represent measurements of the doped samples. The inset shows the absolute Br(79) counts for the undoped sample and the doped samples (blue). The absolute bromine count rate increases with the nominal bromine amount in each sample indicating that the absolute amount of bromine increases which is consistent with the XRF data.

A significant decrease in absolute sample flow rate during the measurement could be observed. The decrease was quantified by the absolute Rh(103) counts which decreased about 30% during the measurement. This is due to blockage of the capillaries and cannot be avoided. However, the absolute count rate is related to the measured Cu/Se ratio due to mass load effect. Therefore a calibration curve for the Cu/Se ratio vs the absolute Rhodium counts had to be created. This was done for the undoped sample by measuring the Cu/Se ratio at the beginning and at the end of the experiment as well as between the measurements of samples with a different Br content (Figure S5). Each measurement consists of 180 scans with a sample time of 0.002 s per scan for each isotope. Washout time between each measurement was 120 s. Afterwards, the relative difference of the Cu/Se ratio between the doped samples and the calibration curve were determined and used to calculate the relative stoichiometry.

Table S1. Relative composition of $Cu_{2-y}Se_{1-x}Br_x$ with respect to the undoped sample with the nominal composition $Cu_{2-\delta}Se$. First, the ratio of selenium versus bromine has been determined for the investigated samples by x-ray fluorescence (XRF) analysis. Second, relative changes in the copper to selenium ratio could be determined using inductively coupled plasma mass spectroscopy (ICP-MS).

x nominal	**x (XRF)**	**1-x (XRF)**	**y (ICP-MS)**
0.00	0.000	1.000	0
0.02	0.022	0.978	0.005
0.03	0.032	0.968	0.030
0.04	0.043	0.957	0.027
0.05	0.058	0.942	0.037
Δ	0.001		0.014

Table S2. Operating parameters for the ELEMENT2 ICP-MS for trace element analysis.

Operating Parameters	
Rf power / W	1105
Cool gas flow rate / l min^{-1}	16
Auxilary gas flow rate / l min^{-1}	0.9
Sample gas / l min^{-1}	0.735
Sample time / s	0.002
Samples per peak	100
Mass window / %	10
Scan mode	Escan
Detector mode	Both (Analog + Counting)

Speed of sound data, densities and results of the SPB model at 550 K in $Cu_{2-y}Se_{1-x}Br_x$. The SPB model was also applied to transport data on $Cu_{2-y}Se_{1-x}Br_x$ at 550 K. The results are shown in Figure S6. The effective masses of $Cu_{2-\delta}Se$ and of the Br-doped samples are increased relative to the values at 305 K.

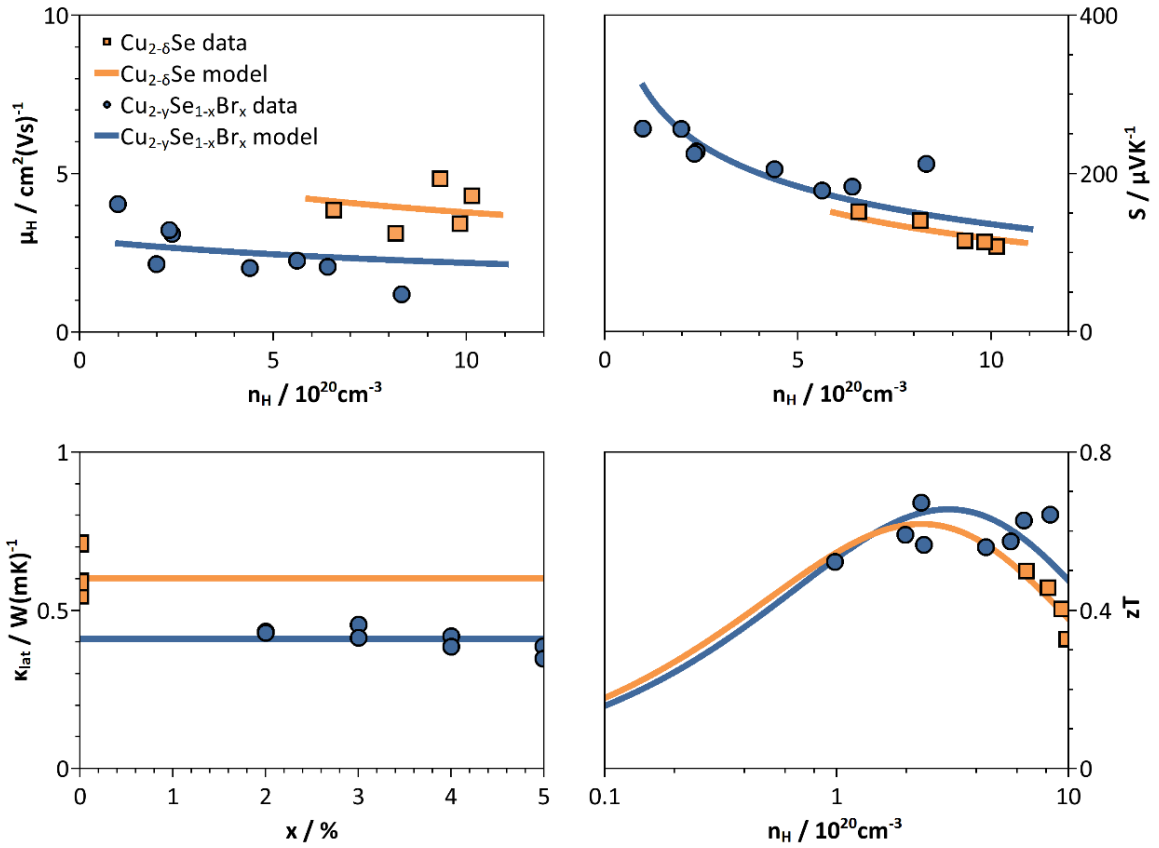

Figure S6. Results for the SPB model with acoustic phonon scattering for $Cu_{2-\delta}Se$ and $Cu_{2-y}Se_{1-x}Br_x$ at 550 K. Orange symbols denote $Cu_{2-\delta}Se$ and blue symbols denote $Cu_{2-y}Se_{1-x}Br_x$. In contrast to the results at 300 K the Hall mobility is not rising with the Hall carrier concentration for the bromine doped samples butt follows the expected trend for acoustic phonon scattering. This is in line with expectations as the relaxation time of acoustic phonon scattering depends on $T^{-3/2}$, whereas that for alloy scattering depends on $T^{-1/2}$. Therefore acoustic phonon scattering will dominate the total charge carrier relaxation time at high temperatures.

This increase in effective mass is responsible for the reduction in μ_0 in $Cu_{2-y}Se_{1-x}Br_x$ relative to $Cu_{2-\delta}Se$ at 550 K; μ_0 depends on $m^{*-5/2}$. The trend of the Hall mobility rising with carrier concentration in the Br-doped samples at 305 K is gone at 550 K. At the higher temperature, the Hall mobility decreases with Hall carrier concentration, as expected for acoustic phonon scattering. This is because the relaxation time for acoustic phonon relaxation time will be much shorter and will dominate the total scattering rate.

Table S3. Densities and speeds of sound data of $Cu_{2-\delta}Se$ and $Cu_{2-y}Se_{1-x}Br_x$ at room temperature. V_l represents the longitudinal speed of sound, v_t represents the transverse speed of sound.

x nominal	d kgm^{-3}	v_l ms^{-1}	v_s ms^{-1}
0.00	6618	3250	1860
0.02	6530	3250	1270
0.03	6542	2700	1350
0.04	6444	2900	1270
0.05	6336	2640	1270

The lower lattice thermal conductivity of the Br-doped samples (0.4 $W(Km)^{-1}$ versus 0.6 $W(Km)^{-1}$) gives them a slight edge over $Cu_{2-\delta}Se$ in maximum zT at 550 K, as shown by the predicted zT versus Hall carrier concentration curves in the bottom right plot of Figure 5. The SPB results for $Cu_{2-y}Se_{1-x}Br_x$ at all temperatures at which the SPB model was applied are shown in Table S3.

Table S4. SPB results for $Cu_{2-y}Se_{1-x}Br_x$ for different temperatures.

T / K	m^* / m_e		μ_0 / $cm^2(Vs)^{-1}$		κ_{lat} / $W(mK)^{-1}$	
	a	**b**	**a**	**b**	**a**	**b**
305	2.1	2.1	34	17	0.16	0.20
350	2.3	2.4	23	12	0.31	0.30
400	3.0	2.5	12	9.1	1.3	0.68
450	2.7	3.2	11	5.5	1.0	0.58
500	3.1	3.8	8.1	3.9	0.61	0.42
550	3.5	4.3	6.1	3.3	0.60	0.41

Doping efficiency calculations. The doping efficiency has been calculated from the average numbers of the charge carrier concentrations for each sample. The expected carrier concentration has been calculated using the crystal structure of high temperature $Cu_{2-\delta}Se$.[18] a represents $Cu_{2-\delta}Se$, b represents $Cu_{2-y}Se_{1-x}Br_x$.

Table S5. Measured and expected charge carrier concentration for $Cu_{2-y}Se_{1-x}Br_x$. Here, the expected charge carrier concentration represents 100 % doping efficiency with respect to the undoped sample. With the relative differences to the undoped sample the doping efficiency for the measured carrier concentrations can be calculated.

x / %	cc (measured) / $10^{20}cm^{-3}$	cc (expected) / $10^{20}cm^{-3}$	Doping efficiency / %
0	4.9	4.9	0
2.2	2.7	0.3	48
3.2	1.9	-1.7	44
4.3	1.5	-4.0	38
5.8	0.9	-7.1	33

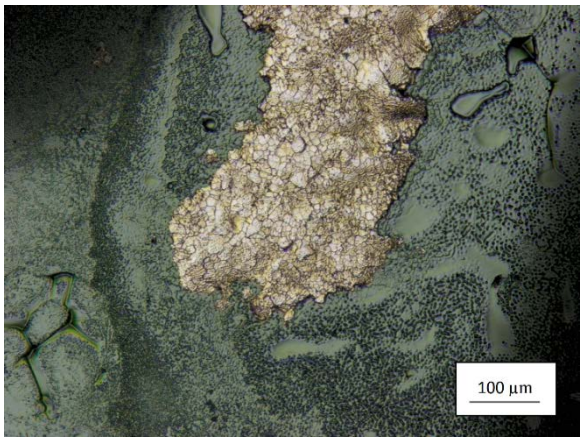

Figure S7. Laser microscope image of excess copper on the surface of the copper selenide chunk after the annealing process. The copper can be easily separated from the chunk using tweezers. Afterwards the surface is removed with sand paper.

Lattice thermal conductivity. The lattice thermal conductivity can be calculated by $\kappa_{lat} = \kappa - \kappa_{el}$ with the total thermal conductivity κ and the electronic contribution to the thermal conductivity κ_{el} which is given by the Wiedemann-Franz law via $\kappa_{el} = L\sigma T$. Here L is the Lorentz number ($2.0 \times 10^{-8}\ W\Omega^{-2}$) and σ the electrical conductivity. Using ultrasonic measurements of longitudinal and transverse sound velocities at room temperature the Debye temperature Θ_D was estimated to be 250 K via,[II]

$$\Theta_D = \frac{v_m \hbar}{k_B}\left(\frac{6\pi^2}{V}\right)^{1/3}$$

where V is the average volume per atom and v_m is the average speed of sound.[III] According to Cahill's formulation, the glassy limit for the thermal conductivity κ_{min} can be estimated.[IV,V] The high temperature limit for the minimum lattice thermal conductivity is given by

$$\kappa_{min} = \frac{1}{2}\left(\frac{\pi}{6}\right)^{1/3} k_B V^{-2/3}(2v_t + v_l)$$

leading to a value of κ_{min}=0.62 W(Km)$^{-1}$. The calculated value of κ_{min} is higher than the lattice thermal conductivity at room temperature, which has also been observed in Cu_2S below the superionic phase transition.[VI]

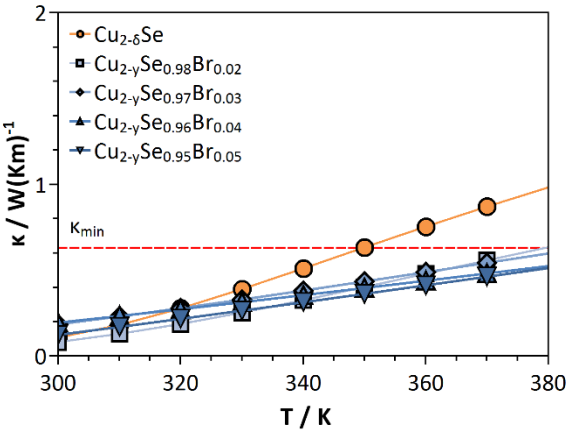

Figure S8. Temperature dependences of the lattice thermal conductivity κ_{lat} in $Cu_{2-y}Se_{1-x}Br_x$, which has been estimated from the Wiedemann-Franz law. The glassy limit of the lattice thermal conductivity κ_{min} has been determined by Cahill's formulation and is represented by the red dotted line.

Ionized impurity scattering. It should be noted, however, that another possible scattering mechanism could be ionized impurity scattering, which would express itself as an increase of the Hall carrier mobility at higher carrier concentrations, due to screening effects.[VII] One might think that ionized impurity scattering would play a role in $Cu_2Se_{1-x}Br_x$ due to the charge differences in Se^{2-} and Br^- and an upward trend of μ_H with n_H can indeed be seen. A combined acoustic phonon and ionized impurity scattering model was applied to the data at 305 K using the equation for the ionized impurity scattering relaxation time and 11.6 for the relative permittivity of $Cu_2Se_{1-x}Br_x$.[VIII]

$$\tau_{ion} = \frac{16\sqrt{2m^*}\pi\chi^2(kT)^{3/2}\epsilon^{3/2}}{N_i Z^2 e^4 g}$$

The S versus n_H data along with curves resulting from combining acoustic phonon scattering with ionized impurity and alloy scattering are shown in Figure S9. Ionized impurity scattering is known to increase the Seebeck coefficient relative to that for acoustic phonon scattering.[IX, X] At the lowest values of n_H measured in $Cu_2Se_{1-x}Br_x$, where ionized impurity scattering would have the greatest effect, the Seebeck curve generated by the combined acoustic phonon and ionized impurity scattering model predicts Seebeck coefficients up to 25 % greater than those actually observed. This systematic over-prediction of the Seebeck coefficient rules out the presence of ionized impurity scattering in this material. This is encouraging because it suggests that doping with something other than Br may not affect the mobility parameter possibly leading to larger quality factors and figures of merit, whereas ionized impurity scattering implies that any dopant would reduce μ_0 and therefore reduce the maximum potential zT.

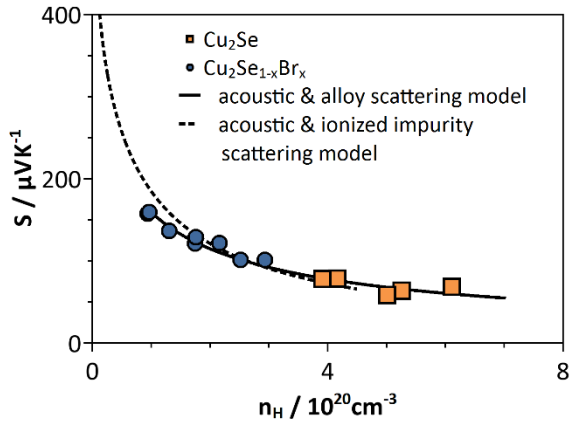

Figure S9. Pisarenko plot of both undoped (orange squares) and doped (blue circles) copper selenide samples at 305 K. The black solid line represents the predicted curve for the combined acoustic and alloy scattering model and the black dashed line for the combined acoustic and ionized impurity scattering model. The overestimation of the Seebeck coefficient at low carrier concentrations rules out ionized impurity scattering.

(I) Puri, S.; Chand, B.; Mehta, D.; Garg, M. L.; Singh, N.; Trehan, P. N. K and L shell X-ray fluorescence cross sections. *Atomic Data and Nuclear Data Tables* **1995**, *61*, 289.
(II) Anderson, O. J. A simplified method for calculating the Debye temperature from elastic constants. *Phys. Chem. Solids* **1963**, *24*, 909.
(III) Toberer, E. S.; Zevalkink, A.; Snyder, G. J. Phonon engineering through crystal chemistry. *J. Mater. Chem.* **2011**, *21*, 15843.
(IV) May, A. F.; Snyder, G. J. In Thermoelectrics Handbook: Thermoelectrics and its Energy Harvesting; Rowe, D. M., Ed.; CRC Press: Boca Raton, FL, 2012; Chapter 11.
(V) Cahill, D.; Watson, S.; Pohl, R. Lower limit to the thermal conductivity of disordered crystals. *Phys. Rev. B* **1992**, *46*.
(VI) He, Y.; Day, T.; Zhang, T.; Liu, H.; Shi, X.; Chen, L.; Snyder, G. J. High Thermoelectric Performance in Non-Toxic Earth-Abundant Copper Sulfide. *Adv. Mater.* **2014**, *26*, 3974.
(VII) Chattopadhyay, D.; Queisser, H. Electron scattering by ionized impurities in semiconductors. J. *Rev. Mod. Phys.* **1981**, *53*, 745.
(VIII) O. Madelung, U. Rossler, and M. Schulz, *in Copper selenides (cu2se, cu(2-x)se) optical and further properties. Non-Tetrahedrally Bonded Elements and Binary Compounds I*, volume 41C *of Landolt-Börnstein-Group III Condensed Matter*, chapter 77, pages 1-6. Springer Berlin Heidelberg, 1998.
(IX) Semiconductor Thermoelements and Thermoelectric cooling. Infosearch, London, 1960.
(X) H. J. Goldsmid in *Proceedings ICT 07: Twenty-sixth international conference on Thermoelectrics*, International Thermoelectrics Society, pages 362-365, 2007**.**
.